

Single-step fabrication and characterization of photonic crystal biosensors with polymer microfluidic channels

Charles J. Choi and Brian T. Cunningham*

Received 8th March 2006, Accepted 19th July 2006

First published as an Advance Article on the web 8th August 2006

DOI: 10.1039/b603514k

A method for simultaneously integrating label-free photonic crystal biosensor technology into microfluidic channels by a single-step replica molding process is presented. By fabricating both the sub-micron features of the photonic crystal sensor structure and the $>10\ \mu\text{m}$ features of a flow channel network in one step at room temperature on a plastic substrate, the sensors are automatically self-aligned with the flow channels, and patterns of arbitrary shape may be produced. By measuring changes in the resonant peak reflected wavelength from the photonic crystal structure induced by changes in dielectric permittivity within an evanescent field region near its surface, detection of bulk refractive index changes in the fluid channel or adsorption of biological material to the sensor surface is demonstrated. An imaging detection instrument is used to characterize the spatial distribution of the photonic crystal resonant wavelength, gathering thousands of independent sensor readings within a single fluid channel.

Introduction

Recently, microfluidic lab-on-a-chip (LOC) devices and micro-total-analysis systems (μTAS) have been investigated in an effort to advance and simplify complex biochemical detection protocols for genomics, proteomics, high-throughput pharmaceutical compound screening, and clinical diagnostic/biomedical applications on a small chip.^{1–3} The need for an automated μTAS to measure large numbers of biochemical interactions is currently being driven by industries and biological research worldwide.^{4,5} To operate a microfluidic system and carry out large numbers of complex biochemical protocols, incorporation of sensors for feedback control and detection of biochemical interactions for process monitoring and verification is essential.

For the majority of assays currently performed, fluorescent or colorimetric chemical labels are commonly attached to the molecules under study so they may be readily visualized.^{6–8} However, using labels induces experimental uncertainties due to the effect of the label on molecular conformation, blocking of active binding epitopes, inaccessibility of the labeling site, or the inability to find an appropriate label that functions equivalently for all molecules in an experiment.⁹ Therefore, the ability to perform highly sensitive biochemical detection without the use of fluorescent labels would further simplify assay protocols, and would provide quantitative kinetic data, while removing experimental artifacts from fluorescent quenching, shelf life and background fluorescence phenomena.¹⁰ While label-free biosensors have been incorporated within separately attached flow channels in the past, most systems are linked to a small number of independent sensor regions. What is needed is a sensor that enables highly parallel

detection of biochemical interactions with a high area density of independent sensors that can function without crosstalk. Ideally, such a system could be easily integrated with a fluid flow network without the need to align the sensors with the flow channels. Ultimately, sensors distributed throughout a chip will be capable of monitoring hundreds of biochemical interactions, and providing real-time feedback to an integrated flow control system.

Previously, label-free optical biosensors based upon a subwavelength photonic crystal structure have been demonstrated.^{11–13} Because the photonic crystal structure does not allow lateral propagation of resonantly coupled light, a single photonic crystal surface is capable of supporting a large number of independent biosensor measurements without optical crosstalk between adjacent sensor regions.¹⁴ Using an image-based sensor readout method, we have demonstrated biosensor image pixel resolution as low as $9 \times 9\ \mu\text{m}^2$, and have applied the imaging method to detect microarray spots, individual cells, and self-referenced assays within 96-well microplates.^{14–16} The photonic crystal surface has been produced over large surface areas from continuous sheets of plastic film, and has been incorporated into single-use disposable 96, 384, and 1536-well microplates (all of which can be imaged for biochemical binding density at $9 \times 9\ \mu\text{m}^2$ pixel resolution over their entire surface area).¹⁵

In this paper, we present for the first time a novel technique for integrating label-free photonic crystal biosensor technology into microfluidic networks by replica molding photonic crystal sensors and fluid channels simultaneously. This approach enables detection modalities such as label-free biochemical detection, sample bulk refractive index detection, and fluid presence within microchannels. By fabricating multiple parallel channels in close proximity, high throughput biochemical assays are enabled. Accurate correction of common-mode error sources such as temperature and bulk solution refractive index variability is enabled by using

Department of Electrical and Computer Engineering, University of Illinois at Urbana-Champaign, Nano Sensors Group, Micro and Nanotechnology Laboratory, 208 N. Wright St., Urbana, IL 61801, USA. E-mail: bcunning@uiuc.edu

sensors embedded in one of the parallel channels as a reference.

The single-step integration of photonic crystal biosensor structures into microfluidic channels presented here is also performed upon flexible plastic substrates using a replica molding approach. This technique enables a simple low-cost manufacturing process to produce sensors and flow channels of arbitrary shape that are automatically aligned to each other. Disposable plastic chips would be less expensive than reusable glass devices and would eliminate time-consuming regeneration steps. In addition, the polymer used for the molded structure has superior solvent resistance and gas permeability properties as compared to polydimethylsiloxane (PDMS), where incompatibility with most organic solvents has limited its use to aqueous-based applications.¹⁷ Finally, through the use of an image-based detection approach, this system is capable of observing the spatial profile of biochemical binding within the fluid channel, both across the channel width, and along the channel length.

Materials and methods

Photonic crystal biosensor

A new class of optical biosensors based on the unique properties of optical device structures known as “photonic crystals” has recently been developed.^{11,18} A photonic crystal is composed of a periodic arrangement of dielectric material in two or three dimensions.^{19,20} If the periodicity and symmetry of the crystal and the dielectric constants of the materials used are chosen appropriately, the photonic crystal will selectively couple energy at particular wavelengths, while excluding others.²¹ The applications of structures such as these are numerous, including integration with lasers to inhibit or enhance spontaneous emission, waveguide angle steering devices, and as narrowband optical filters.^{22–26} A photonic crystal structure geometry can be designed to concentrate light into extremely small volumes and to obtain very high local electromagnetic field intensities.

In order to adapt a photonic crystal device to perform as a biosensor, some portion of the structure must be in contact with a liquid test sample. By attaching biomolecules or cells to the portion of the photonic crystal where the locally confined electromagnetic field intensity is greatest, the resonant coupling of light into the crystal is modified, so the reflected/transmitted output is tuned. The highly confined electromagnetic field within a photonic crystal structure provides high sensitivity and a high degree of spatial resolution consistent with their use in imaging applications, much like fluorescent imaging scanners.

Photonic crystal structures have their historical roots in a phenomenon called “Wood’s Anomaly.” Wood’s Anomalies are effects observed in the spectrum of light reflected by optical diffraction gratings.²⁷ They manifest themselves as rapid variations in the intensity of particular diffracted orders in certain narrow frequency bands. They were first discovered by Robert W. Wood in 1902 during some of the first experiments on reflection gratings and were termed “anomalies” because the effects could not be explained by ordinary grating theory. Since that time, optical theory and numerical methods have

developed so that structures making use of similar optical effects could be engineered to produce useful devices in the fields of telecommunications and optical displays.²⁸ For example, subwavelength periodic structures have been developed to reflect only a very narrow band of wavelengths when illuminated with white light.²⁵ To create a biosensor, a photonic crystal may be optimized to provide an extremely narrow resonant mode whose wavelength is particularly sensitive to modulations induced by the deposition of biochemical material on its surface.¹¹ A sensor structure consists of a low refractive index plastic material with a periodic surface structure that is coated with a thin layer of high refractive index dielectric material. The sensor is measured by illuminating the surface with white light, and collecting the reflected light with a non-contact optical fiber probe, where several parallel probes can be used to independently measure different locations on the sensor. The biosensor design enables a simple manufacturing process to produce sensor sheets in continuous rolls of plastic film that are hundreds of metres in length.¹² The mass manufacturing of a biosensor structure that is measurable in a non-contact mode over large areas enables the sensor to be incorporated into single-use disposable consumable items such as 96, 384, and 1536-well standard microplates, thereby making the sensor compatible with standard fluid handling infrastructure employed in most laboratories.

The sensor operates by measuring changes in the wavelength of reflected light as biochemical binding events take place on the surface. For example, when a protein is immobilized on the sensor surface, an increase in the reflected wavelength is measured when a complementary binding protein is exposed to the sensor. Using low-cost components, the readout instrument is able to resolve protein mass changes on the surface with resolution less than 1 pg mm^{-2} . While this level of resolution is sufficient for measuring small-molecule interactions with immobilized proteins, the dynamic range of the sensor is large enough to also measure larger biochemical entities including live cells, cell membranes, viruses, and bacteria. A sensor measurement requires $\sim 20 \text{ ms}$, so large numbers of interactions can be measured in parallel, and kinetic information can be gathered. The reflected wavelength of the sensor can be measured either in “single point mode” (such as for measuring a single interaction within a microplate), or an imaging system can be used to generate an image of a sensor surface with $< 9 \text{ }\mu\text{m}$ resolution. The “imaging mode” has been used for applications that increase the overall resolution and throughput of the system such as label-free microarrays, imaging plate reading, self-referencing microplates, and multiplexed spots/wells.¹⁴

Microfluidic sensor fabrication

The fabrication process requires a method that can accurately produce sub-micron features for the photonic crystal structure, while at the same time producing the $> 10 \text{ }\mu\text{m}$ features of the microfluidic channel. A replica-molding process using a rigid “master” structure and a UV-curable liquid polymer material were selected for this purpose because the molding may be performed at room temperature without the need to exert a

large force between the mold and the molded material. An outline of the fabrication procedure is shown in Fig. 1a.

First, a silicon master wafer with 550 nm period 1-D linear grating structures was fabricated. The grating structures were patterned with photoresist using deep-UV lithography, in which 6.7 mm diameter circular dies were stepped and repeated every 9 mm. After the exposed photoresist was developed, the

patterned grating structure was transferred to the silicon wafer by reactive ion etching to a depth of approximately 170 nm. After etching, the photoresist was removed. Next, the fluid channel structures were patterned onto the same silicon master wafer with grating structures from the previous step using photoresist again, but with conventional lithography. Because high resolution is not required for defining the channels (channel widths of 30–250 μm were investigated), and to maximize flexibility for investigating different channel shapes, the photomask for the channel patterns was produced upon a transparent plastic sheet with 5080 dpi high resolution printing. After developing the exposed photoresist, channel structures were transferred onto the silicon wafer using deep reactive ion etching with a depth of approximately 20 μm , followed by removal of the photoresist. As a result, a negative pattern template of microfluidic channels incorporated with sub-micron scale linear grating structures was formed. Subsequently, the completed silicon template was treated with repel silane (GE Healthcare) to promote clean release of the replica from the template without contaminating the template structures with polymer residues.

Utilizing the silicon master wafer as a mold, the surface structure of the master wafer was replicated onto a 250 μm thick flexible polyethylene terephthalate (PET) substrate by distributing a layer of liquid UV curable polymer between the silicon master wafer and the PET substrate. The liquid polymer conforms to the shape of the features on the master wafer, and is subsequently cured to a solid state by exposure to UV light. After the polymer was cured, the surface structure was peeled away from the silicon wafer, leaving behind a replica of the silicon master wafer surface adhered to the PET sheet. The sensor was completed by depositing approximately 150 nm of titanium dioxide (TiO_2) using electron beam evaporation on the replica surface. The SEM images in Fig. 1b show the cured replica surface coated with TiO_2 , in which the replicated flow channel contains the photonic crystal biosensor on its bottom surface.

The upper surface of the microfluidic channel was applied by sealing with a separate PET sheet with inlet and outlet holes, using a layer of 2-sided pressure-sensitive film adhesive (3M) in between. The sealed plastic microfluidic sensor chip was then attached with the same transparent film adhesive to the surface of a $1 \times 3 \text{ inch}^2$ glass microscope slide to provide structural rigidity. The microfluidic sensor chip was completed by attaching polypropylene (PP) flow connectors on the inlet holes of the PET cover layer using an adhesive, followed by reinforcement sealing with clear epoxy. Flowing fluids into the

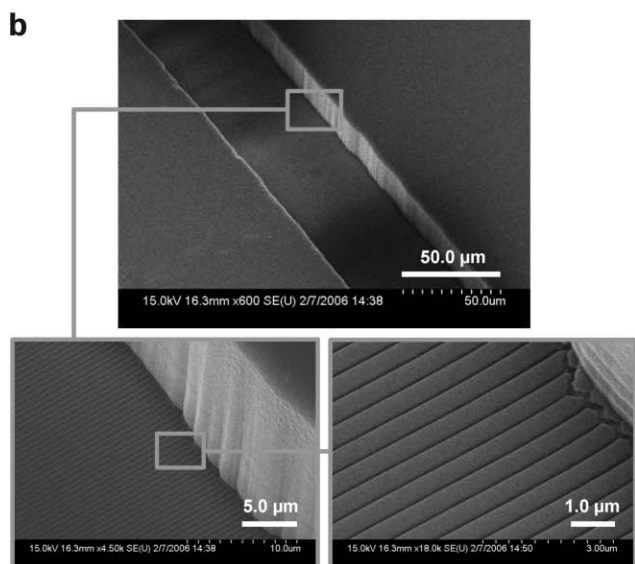
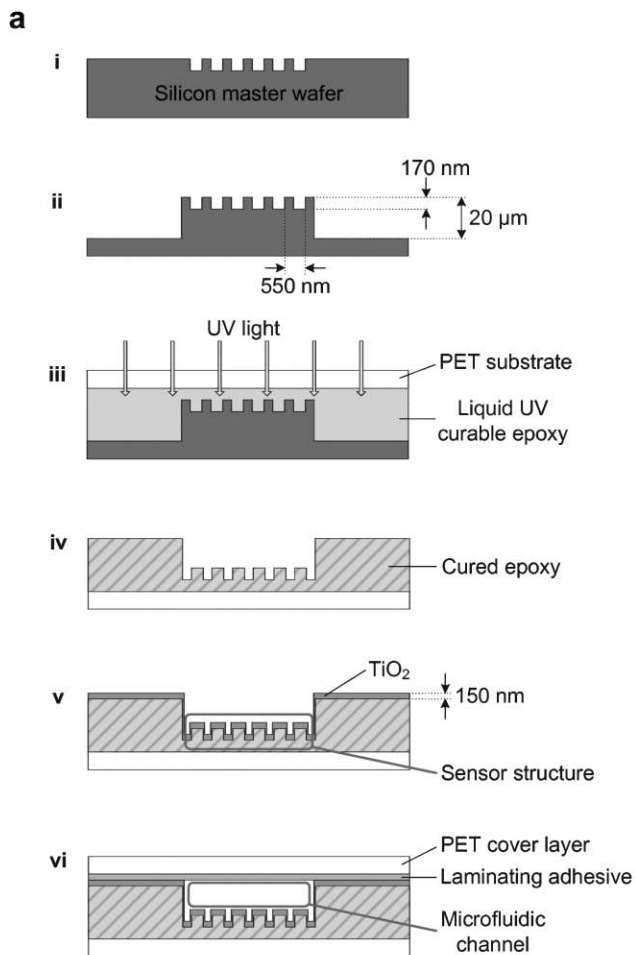


Fig. 1 (a) Fabrication process used to produce the microfluidic sensor chip. (i) A silicon master wafer with grating structures was fabricated. (ii) Micro scale fluid channel structures were patterned onto the same silicon master wafer. (iii) Microfluidic channels integrated with grating structures were replicated onto a PET substrate with UV curable epoxy and subsequent exposure to UV light. (iv) The cured replica was released from the silicon wafer onto the PET sheet. (v) 150 nm of TiO_2 was deposited onto the replica. (vi) Exposed microfluidic channels embedded with sensor structures were sealed with a separate PET sheet, using a layer of laminating adhesive in between. (b) Scanning electron micrograph of microfluidic channels embedded with photonic crystal biosensor.

microfluidic channels was accomplished by pre-filling the PP flow connectors with solutions or analytes and manually pumping it using a syringe with tubing connected to the PP flow connector. A manual syringe pumping method was sufficient because experiments performed in this work involved filling the channels with solutions, incubating/stabilizing at room temperature, washing/rinsing with buffer, and therefore were independent of fluid flow rate.

Imaging instrument

A schematic diagram of the biosensor peak wavelength value (PWV) imaging instrument is shown in Fig. 2. White light illuminates the sensor at normal incidence with a polarization filter to apply only light with a polarization direction perpendicular to the sensor grating lines. The reflected light is directed through a beam splitter and an imaging lens of unity magnification to a narrow slit aperture at the input of an imaging spectrometer. The width of the slit may be set at a desired value, *e.g.* within a range from 6 to 200 μm . Using this method, reflected light is collected from a line on the sensor surface, where the width of the imaged line is determined by the width of the entrance slit of the imaging spectrometer. The imaging spectrometer contains a two-dimensional CCD camera (Acton Research) with 2048×512 pixels. The line of reflected light, containing the biosensor resonance signal, is diffracted by a diffraction grating to produce a spatially-resolved spectrum from each point within the line. When the CCD camera is operated in 2048×512 pixel mode, the line-image through the slit is imaged onto 512 pixels. A spectrum, with a resolution of 2048 wavelength data points, is acquired for each of the 512 pixels. Upon peak-finding analysis of all 512 spectra, the PWVs of 512 pixels are determined. Thus, a line of 512 pixels is generated for the PWV image of the sensor.

To generate a 2-D PWV image of the sensor, a motorized stage translates the sensor which is placed on a precise holding fixture, in the direction that is perpendicular to the image line. The spatial separation of the image lines is determined by the step-size of the stage between each image-line acquisition (in addition, the CCD can be read out with various resolutions by binning pixels). By this technique, a series of lines are assembled into an image through software and the same spot

in the sensor can be scanned repeatedly after the sensor has been translated. In the current system, the length of the image line is 9.1 mm, as determined by the size of the CCD chip, across the biosensor surface. A large area can be scanned in a tiled fashion, where the width of a tile is 9.1 mm, by translating the sensor in steps of 9.1 mm along the image-line direction.

Typically, a biosensor experiment involves measuring shifts in PWV so the sensor surface is scanned twice; once before and once after biomolecular binding. The images are aligned and subtracted to determine the difference in PWV as detected by the sensor. This scanning method does not require the PWV of the imaged surface to be completely uniform, either across the surface or within a set of probe locations, or tuning of the sensor angle to a resonance condition as with SPR imaging.²⁹

Results and discussion

Bulk refractive index sensitivity experiment

The sensor structure integrated within the fluid channels measures changes in dielectric permittivity upon its surface. Therefore, flowing liquid solutions with variable refractive index through the fluid channels induces a PWV shift. Because refractive index corresponds linearly with dimethyl sulfoxide (DMSO) concentration in DI water, the dependence of PWV on bulk refractive index was determined by flowing in different concentrations of DMSO solution in DI water to the fluid channels. Initially, all three channels were filled with DI water and a baseline PWV imaging scan at 22.3 μm resolution was made using the instrument. The resulting spatial PWV image is shown in Fig. 3a, in which PWVs are represented by the scale bar ranging from 870 nm to 880 nm with the red region representing areas of higher PWV. Fig. 3b shows sample reflection spectra from one data pixel from each channel with PWV of 877.79, 877.65, 876.87 nm for p1, p2 and p3, respectively. Fig. 3c and 3d are cross section plots of the spatial PWV image. The plot in Fig. 3c represents PWVs along the green horizontal cross section line and likewise, Fig. 3d represents PWVs along the orange vertical cross section line. The cross section PWV plots indicate that the PWVs vary slightly from different channels and even within the same channel. This is acceptable since quantity of interest in this case is the shift in PWV when different solutions are introduced or some biochemical reaction occurs on the sensor surface, rather than the PWV itself.

After taking a PWV image scan with the channels filled with DI water, channels 1 and 3 were filled with DMSO solution while channel 2 was refilled with DI water, to serve as a reference. Fig. 4a shows a spatial PWV shift image measured by flowing 6.25% DMSO solution through channels 1 and 3. A shifted PWV image is obtained by subtracting the reference spatial PWV image with all channels filled with DI water (Fig. 3a) from the spatial PWV image of the exact same device filled with 6.25% DMSO solutions in channels 1 and 3. Therefore, PWV variations caused by the fabrication non-uniformity shown in Fig. 3 do not result in significant sensitivity non-uniformity as PWV image subtraction is performed. PWV shifts are represented by the scale bar from -0.2 to 2.7 nm where red regions represent areas of greatest

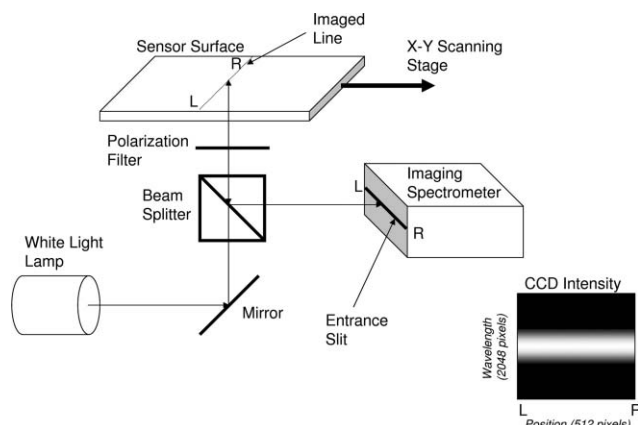


Fig. 2 Schematic diagram of the imaging readout instrument.

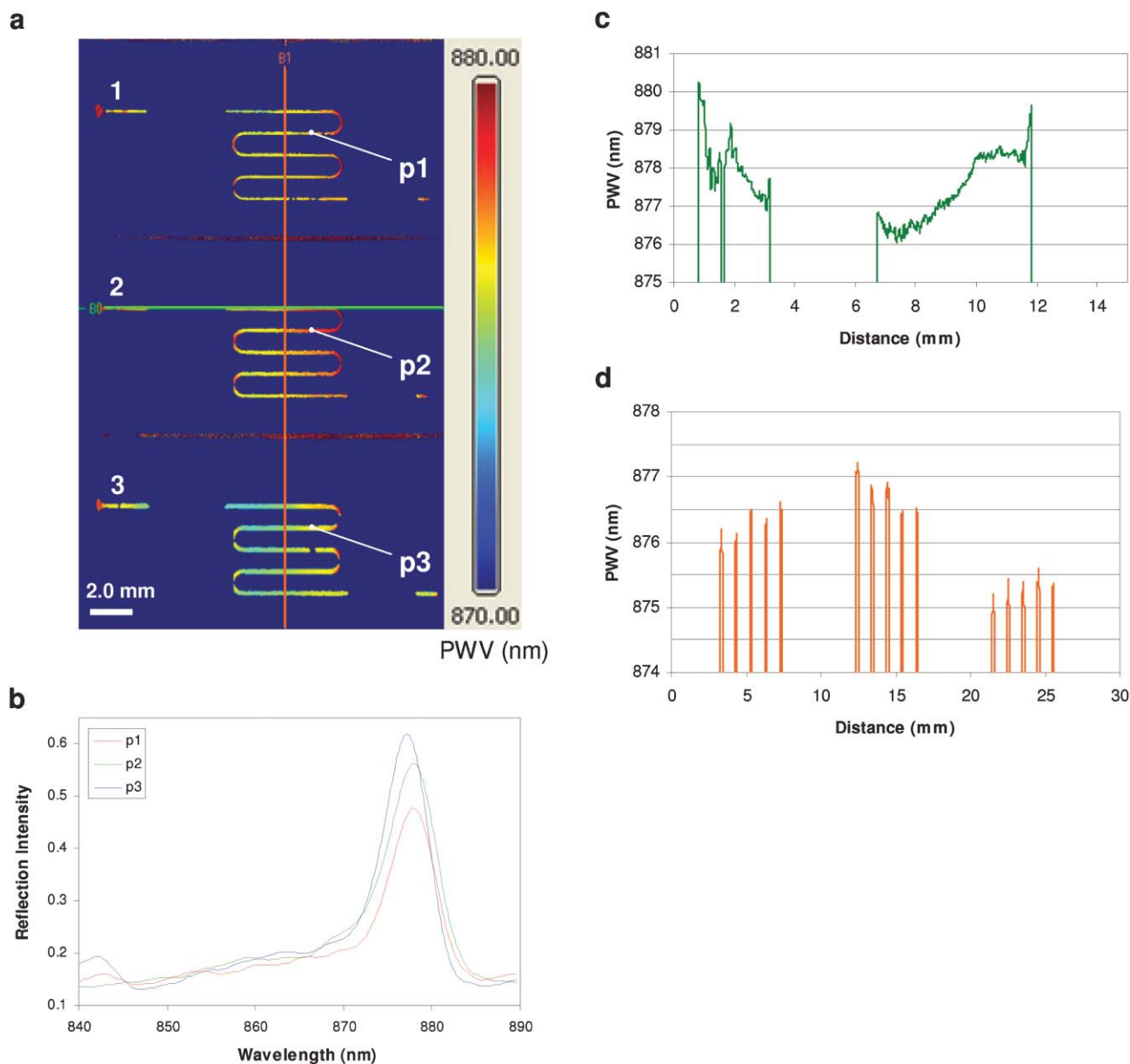


Fig. 3 PWV data gathered by the imaging instrument with all three fluid channels filled with DI water. (a) Spatial PWV image of the channels. PWV shifts are represented by the scale bar ranging from 870 nm to 880 nm. (b) Sample reflection spectra of one data pixel from each of the three channels. (c) Horizontal cross section plot representing PWVs along the green horizontal cross section line in (a). (d) Vertical cross section plot representing PWVs along the vertical orange cross section line in (a).

positive shift. The overall standard deviation for the shifted PWV of the data was 0.263 nm.

Once the shifted PWV images are obtained, grids of sensor regions are selected (square areas in Fig. 4a) where many independent pixel readings within each grid can be averaged into a single measurement. A masking function is applied so that only resonant peaks with reflected intensity maxima above a user-selectable value are considered for the selection of spectra within the grid. Through the masking function, therefore, regions of the chip that do not contain a photonic crystal structure (such as the regions between flow channels) that do not reflect a resonant peak, are automatically eliminated from further consideration. Each grid can be

designated as “active” or “reference”, and PWV shifts from reference regions can be associated with any desired active region for subtraction of common-mode artifacts. In this experiment, the PWV shift was calculated by subtracting the average PWV shift within the grid of channel 2 (reference), from the average PWV shift of the grids for channels 1 and 3 (active). Because of the differences in channel width (150, 200, and 250 μm for channels 1, 2, and 3, respectively), the number of independent data pixels satisfying the mask function within each grid for channels 1, 2, and 3 were 2560, 4337, and 7509, respectively.

Scans were made after flowing each of the different DMSO concentrations ranging from 0.78% to 25% through channels 1

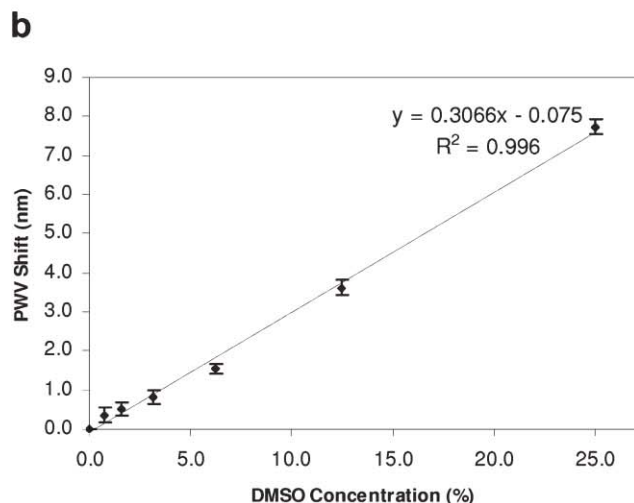
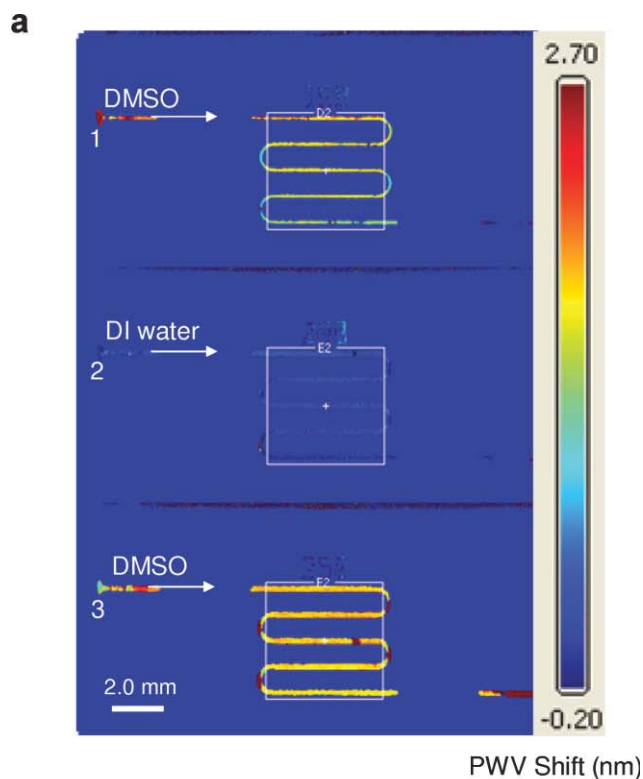


Fig. 4 (a) PWV shift measured by flowing 6.25% DMSO solution through channels 1 and 3, and flowing DI water through channel 2 to serve as a reference. PWV shifts are represented by the scale bar from -0.20 to 2.70 nm where the red regions represent areas of greater positive shift. (b) Plot of PWV shift measured with DMSO solution with a concentration ranging from 0% to 25%, in which the data points were linearly fitted with least squares approximation with an R^2 value equal to 0.996.

and 3. Both channels were rinsed with DI water and dried before flowing in different concentrations of DMSO solutions. Fig. 4b plots the PWV shift as a function of DMSO concentration. The data points were linearly fitted with least squares approximation with an R^2 value of 0.996, showing the expected linear dependence between photonic crystal reflected resonant PWV and the solution bulk refractive index. The

approximate bulk refractive index change corresponding to a 6.25% change in DMSO concentration (Δ PWV of 1.841 nm) is 0.00682, based on the bulk refractive index shift coefficient ($\sigma = \Delta$ PWV/ Δn) value of 270, determined from previous research.¹³

Protein A—Immunoglobulin G (IgG) experiment

An experiment was performed to demonstrate detection of bimolecular binding on the surface of the photonic crystal sensor within the fluid channels. Protein A (Pierce Biotechnology) was used as the immobilized protein ligand on the sensor surface, while chicken IgG and pig IgG (Sigma-Aldrich) were used as analytes. Pig IgG is known to have a strong binding affinity for Protein A, while chicken IgG is known not to bind with Protein A, and therefore acts as a negative control for our experiment.^{30,31}

Before immobilization of Protein A, a baseline PWV image of three channels filled with PBS buffer (Sigma-Aldrich) was taken at a pixel resolution of $22.3 \mu\text{m}$. The Protein A was attached by simple physical adsorption by flowing a 0.5 mg mL^{-1} solution through all three channels, allowing the solution to incubate for 10 min, followed by washing away of unbound Protein A with PBS buffer. A second PWV image was gathered after Protein A immobilization, with PBS buffer in the channels. Next, channel 1 was filled with PBS buffer to serve as a reference, while channels 2 and 3 were filled with 0.5 mg mL^{-1} concentration solutions of chicken IgG and pig IgG respectively. The IgGs were allowed to incubate with the immobilized Protein A for 10 min, followed by a thorough PBS wash to remove unbound IgGs. Then, a final PWV scan was made with all three of the channels filled with PBS buffer. Fig. 5a shows a PWV shift image for subtraction of the PWV image after Protein A coating from the PWV image after IgG binding. PWV shifts are represented by the scale bar from -0.60 to 1.65 nm where red regions represent areas of greatest positive shift. As shown in Fig. 5a, three horizontal lines within each channel (lines 1, 2 and 3 colored in orange, red and blue, respectively) are selected, in which independent PWV shift pixel data along the lines are sampled. The number of independent data pixels sampled within each line is 190 and Fig. 5b is the cross sectional PWV shift plot along lines 1, 2 and 3 for each of the three channels for PBS buffer, chicken IgG, and pig IgG, respectively. In order to calculate the overall PWV shifts for the IgGs, square grids of sensor regions, shown in Fig. 5a are selected, in which many independent pixel PWV data within each grid can be averaged. Again, because of the differences in channel width, the number of independent data pixels sampled within each grid for channels 1, 2, and 3 were 2223, 5449, and 6208, respectively. For this experiment, the overall average PWV shifts for IgGs were calculated by subtracting the average PWV shift within the grid of channel 1, which is the reference, from the average PWV shift of grids for channels 2 and 3 corresponding to chicken IgG and pig IgG, respectively. Using the above method, the average PWV shifts measured and calculated in the chicken IgG and pig IgG containing sensor channels were -0.051 and 0.815 nm, respectively, demonstrating selective attachment of the analyte to the immobilized Protein A.

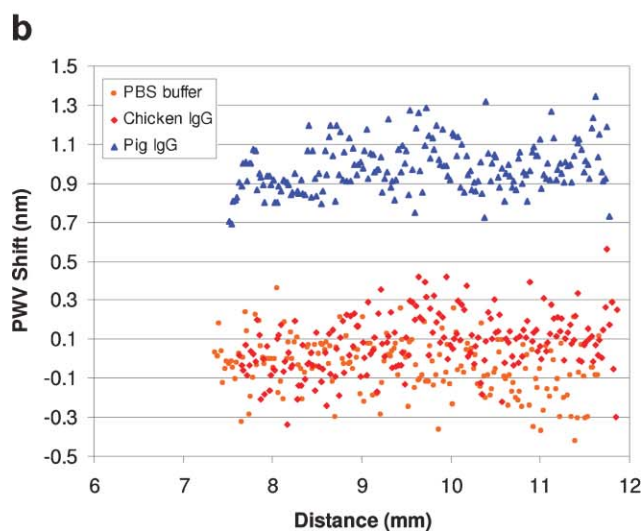
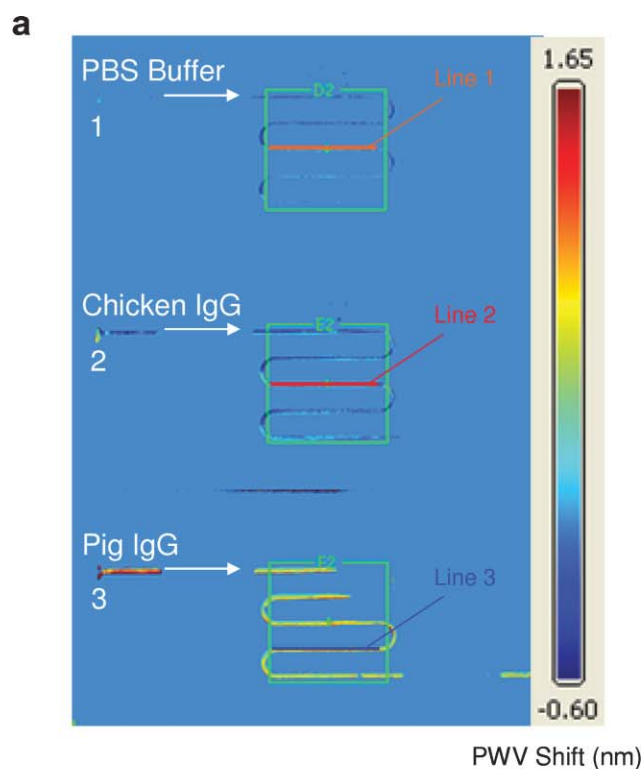


Fig. 5 (a) Shifted PWV image (subtraction of the PWV image of Protein A coated channels from the PWV image with channels 2 and 3 bound with IgG molecules). Amount of shifts are represented by the scale bar from -0.60 to 1.65 nm, where red regions represent areas of greatest positive shift. (b) Cross sectional PWV shift plot along lines 1, 2 and 3 for each of the three channels for PBS buffer, chicken IgG, and pig IgG respectively.

Discussion

The fabrication and detection methods described in this work represent the building blocks that may be used to design and build more sophisticated lab-on-a-chip systems incorporating sensors for label-free biochemical or cellular analysis. This work demonstrates that a narrow photonic crystal region within a flow channel provides a strong resonant reflection

signal, and that a large number of independent “pixels” may be monitored at one time within a small chip. The imaging capability may be utilized in several ways to improve the resolution and/or throughput of label-free measurements. As demonstrated with the serpentine flow channel design, a single “line” of PWV measurements across the width of many flow channels may be used to monitor biochemical binding in a large number of flow channels at one time. Although only “end point” measurements were shown here, a single PWV line may be scanned rapidly (~ 20 ms per scan) to gather kinetic binding data for all the flow channels intersecting the line. Further, PWV measurements are not limited to a single reading across the width of a flow channel, but rather the variability in binding density from the center to the edge of the channel is easily detected. These types of measurements will enable optimization of flow conditions and direct observation of edge effects that are not normally detected. Likewise, the serpentine flow channels allowed us to demonstrate detection of biochemical binding down the length of a single flow channel where, again, rapid scanning will allow direct observation of immobilized ligand density binding variability and detected analyte variability, and any nonuniformity resulting from mass transport limitations. By taking many independent binding readings down the length of a channel, we expect to reduce the statistical (random) noise of individual PWV determinations to extremely low levels through averaging. In the case of our serpentine channel configuration, all the PWV shift readings, with >6000 readings within a single channel for $\sim 22 \times 22 \mu\text{m}^2$ pixels, are easily gathered together to calculate an average PWV shift measurement for the entire channel. In future work, we will investigate how the noise depends on the scanning pixel resolution, and attempt to determine tradeoffs between pixel resolution, chip scan time, and PWV resolution. Further, the method allows reference channels to be incorporated in close physical proximity to active channels for highly accurate correction of temperature or buffer variability. Because active and reference regions are small, many reference regions may be easily incorporated onto a single chip.

In future work, we plan to develop more complex sensor/flow channel configurations that can incorporate valving and mixing capabilities into the chip. We also plan to use this capability not only for biochemical assays, but also for detection of immobilization of larger biological objects, including cells and bacteria for cytotoxicity assays, chemotaxis assays, and diagnostic tests, and cell/bacteria identification.

Conclusion

We have demonstrated a single-step process for integrating the fabrication of photonic crystal biosensors and microfluidic channels. The process enables the submicron structure of the photonic crystal to be replicated simultaneously with the $>10 \mu\text{m}$ structures for the fluid channels, and self-aligns the sensors with the channels. The process is performed using a room-temperature replica molding process that is performed on flexible plastic substrates for low-cost manufacturing. The fabricated sensors may be measured in a high-resolution imaging mode that can obtain information from many

locations within the chip surface simultaneously for monitoring biochemical interactions in a high throughput manner and observation of binding interaction uniformity along the lengths and across the widths of the channels. We demonstrated the ability of the integrated sensors to detect changes in the bulk refractive index of fluid introduced into the channels and to selectively detect an antibody at high concentration with an immobilized ligand. In the current work, flow was used to introduce reagents to the sensors in the channels, but kinetic information was not gathered and measurements were taken in the absence of active flow. We expect to build upon the currently demonstrated capabilities using this process with more sophisticated flow systems for applications in pharmaceutical compound screening, protein–protein interaction characterization, and cell-based assays.

Acknowledgements

The authors gratefully acknowledge the staff of the Micro and Nanotechnology Laboratory at University of Illinois at Urbana-Champaign and the Center for Nanoscale Chemical-Electrical-Mechanical Manufacturing Systems. This material is based upon work supported by the National Science Foundation under NSF DMI 03-28162. Any opinions, findings, and conclusions or recommendations expressed in this material are those of the author(s) and do not necessarily reflect the views of the National Science Foundation.

References

- 1 M. A. Burns, B. N. Johnson, S. N. Brahmaandra, K. Handique, J. R. Webster, M. Krishnan, T. S. Sammarco, P. M. Man, D. Jones, D. Heldsinger, C. H. Mastrangelo and D. T. Burke, *Science*, 1998, **282**, 484–487.
- 2 D. Figeys and D. Pinto, *Electrophoresis*, 2001, **22**, 208–216.
- 3 N. H. Chiem and D. J. Harrison, *Clin. Chem.*, 1998, **44**, 591–598.
- 4 D. A. Dunn and I. Feygin, *Drug Discovery Today*, 2000, **5**, S84–S91.
- 5 N.-T. Nguyen and S. T. Wereley, *Fundamentals and Applications of Microfluidics*, Artech House, Inc., Norwood, MA, 2002.
- 6 A. Pandey and M. Mann, *Nature*, 2000, **405**, 837–846.
- 7 N. L. Anderson, A. D. Matheson and S. Steiner, *Curr. Opin. Biotechnol.*, 2000, **11**, 408–412.
- 8 G. MacBeath and S. L. Schreiber, *Science*, 2000, **289**, 1760–1763.
- 9 A. Brecht and G. Gauglitz, *Biosens. Bioelectron.*, 1995, **10**, 923–936.
- 10 A. J. Cunningham, *Introduction to Bioanalytical Sensors*, John Wiley & Sons, New York, 1998.
- 11 B. Cunningham, P. Li, B. Lin and J. Pepper, *Sens. Actuators, B: Chem.*, 2002, **81**, 316–328.
- 12 B. Cunningham, B. Lin, J. Qiu, P. Li, J. Pepper and B. Hugh, *Sens. Actuators, B: Chem.*, 2002, **85**, 219–226.
- 13 B. Cunningham, J. Qiu, P. Li and B. Lin, *Sens. Actuators, B: Chem.*, 2002, **87**, 365–370.
- 14 P. Y. Li, B. Lin, J. Gerstenmaier and B. T. Cunningham, *Sens. Actuators, B: Chem.*, 2004, **99**, 6–13.
- 15 B. T. Cunningham, P. Li, S. Schulz, B. Lin, C. Baird, J. Gerstenmaier, C. Genick, F. Wang, E. Fine and L. Laing, *J. Biomol. Screen.*, 2004, **9**, 481–490.
- 16 B. Lin, P. Li and B. T. Cunningham, *Sens. Actuators, B: Chem.*, 2006, **114**, 559–564.
- 17 P. J. A. Kenis and A. D. Stroock, *MRS Bull.*, 2006, **31**, 87–90.
- 18 A. J. Haes and R. P. Van Duyne, *J. Am. Chem. Soc.*, 2002, **124**, 10596–10604.
- 19 J. D. Joannopoulos, R. D. Meade and J. N. Winn, *Photonic Crystals*, Princeton University Press, Princeton, NJ, 1995.
- 20 B. A. Munk, *Frequency Selective Surfaces*, John Wiley & Sons, 2000.
- 21 V. Pacradouni, W. J. Mandeville, A. R. Cowan, P. Paddon, J. F. Young and S. R. Johnson, *Phys. Rev. B*, 2000, **62**, 4204–4207.
- 22 S. John, *Phys. Rev. Lett.*, 1987, **58**, 2486–2489.
- 23 S. John and V. I. Rupasov, *Phys. Rev. Lett.*, 1997, **79**, 821–824.
- 24 A. Scherer, T. Yoshie, M. Loncar, J. Vuckovic, K. Okamoto and D. Deppe, *J. Korean Phys. Soc.*, 2003, **42**, 768–773.
- 25 R. Magnusson and S. S. Wang, *Appl. Phys. Lett.*, 1992, **61**, 1022–1024.
- 26 R. Magnusson and S. S. Wang, *Appl. Opt.*, 1995, **34**, 8106–8109.
- 27 R. W. Wood, *Philos. Mag.*, 1902, **4**, 396–402.
- 28 A. Hessel and A. A. Oliner, *Appl. Opt.*, 1965, **4**, 1275–1297.
- 29 E. A. Smith and R. M. Corn, *Appl. Spectrosc.*, 2003, **57**, 320A–332A.
- 30 G. Kronvall and R. C. Williams, *J. Immunol.*, 1969, **103**, 828–833.
- 31 A. Surolia, D. Pain and M. I. Khan, *Trends Biochem. Sci.*, 1982, **7**, 74–76.